Materials Research. 2023; 26:e20230194
DOI: https://doi.org/10.1590/1980-5373-MR-2023-0194

Microstructure and Properties of Al_2O_3-$Y_3Al_5O_{12}$ Reactive Sintered Ceramic Composites with Multilayer Compositional Gradient: an Initial Investigation

Vinícius Z. Bôsco de Souza[a], *Bruno Medeiros da Silva*[a], *Bruno Xavier de Freitas*[b], *José Eduardo Vasconcelos Amarante*[c], *Paula Cipriano da Silva Vidal*[a], *Ésoly Madeleine Bento dos Santos*[a], *Claudinei dos Santos*[a,d]*

[a]*Universidade Federal Fluminense (UFF), Escola de Engenharia Industrial Metalúrgica de Volta Redonda, Volta Redonda, RJ, Brasil.*
[b]*Universidade Federal de Itajubá (UNIFEI), Instituto de Engenharia Mecânica, Itajubá, MG, Brasil.*
[c]*Universidade Federal Fluminense (UFF), Faculdade de odontologia, Instituto de Saúde de Nova Friburgo, Nova Friburgo, RJ, Brasil.*
[d]*Universidade do Estado do Rio de Janeiro (UERJ), Faculdade de Tecnologia de Resende, Resende, RJ, Brasil.*

Received: April 09, 2023; Revised: August 27, 2023; Accepted: October 11, 2023

In this work, mixtures of ceramic powders containing Al_2O_3 with different amounts of Y_2O_3 (1%, 3%, 5% and 10wt.%) along their cross-section were fabricated to obtain multilayer composites based on Al_2O_3 with different levels of $Y_3Al_5O_{12}$ (YAG) as reinforcement. Monolithic cylindrical multilayer Al_2O_3 blocks were compacted and subsequentially, sintered at 1610°C for 4h. Phase stability, microstructural aspects, and physical and mechanical properties of the specimens were acquired by relative density, X-ray diffraction, scanning electron microscopy, Vickers hardness, fracture toughness, Young's modulus and biaxial flexural strength measurements. The results indicated that monolithic alumina specimens exhibited relative density of 98%, with average hardness of 1203 ±83 HV, fracture toughness of 2.1 ±0.8 MPa.m$^{1/2}$ and flexural strength of 187 ±64 MPa. Progressive incorporation of Y_2O_3 into the chemical composition of the specimens led to formation of the YAG phase by solid state reaction during sintering, which reduced hardness and increased densification, fracture toughness and flexural strength, with average values of HV=1023 ±28 HV, K_{IC}=3.5 ±0.3 MPa.m$^{1/2}$, σ_f=273 ±58 MPa and 14% $Y_3Al_5O_{12}$ for the specimens with 10wt.% Y_2O_3. This improvement is probably associated with toughness mechanisms, such as crack deflection and residual thermal stresses between the phases present in the composites.

Keywords: *Multilayer composites, Al_2O_3-$Y_3Al_5O_{12}$ ceramic composite, gradient composition, mechanical properties.*

1. Introduction

Alumina (Al_2O_3)-based ceramics have been widely used in structural engineering applications because of their high wear resistance and hardness and chemical stability at both room and high temperatures[1,2]. Addition of a second phase has been used to improve its mechanical properties. The $Y_3Al_5O_{12}$ (YAG – Yttrium Aluminum Garnet) phase is among the potential candidates for mechanical reinforcement of alumina-matrix ceramics[3-6].

Al_2O_3-$Y_3Al_5O_{12}$ composites have been used as a component in aircraft jet engines and machining tools. Moreover, their mechanical integrity at high temperatures (~1500 °C) has been confirmed by several studies[7-11]. The biphasic microstructure created from the sintering of Al_2O_3 and Y_2O_3 powders boost the formation of homogeneously distributed α-Al_2O_3 grains and YAG phases. In addition, throughout the sintering process, residual thermal stresses between the two phases are generated because of the mismatch of coefficients of thermal expansion (CTE)[12]. Therefore, this behavior increases the fracture strength of Al_2O_3-$Y_3Al_5O_{12}$ composites by limiting intergranular crack propagation[13].

An alternative processing route was proposed to create a ceramic composite with a compositional gradient that combines different properties (e.g., hardness, flexural strength, Young's modulus, etc.) in the same material. This route was investigated in Al_2O_3-ZrO_2 system: multilayer ceramic composites were manufactured based on Al_2O_3 reinforced with different amounts of yttria-stabilized tetragonal zirconia polycrystals (Y-TZP). The results showed improvements in fracture toughness and densification and maintained the aspects characteristic of alumina, such as high hardness and chemical stability, with increasing the Y-TZP reinforcement[14,15].

These functional gradient materials present the advantage of optimization by distributing different microstructures in a single piece[16], and the primary toughness enhancing

*e-mail: claudineisvr@gmail.com

mechanisms of particle reinforced ceramics have been attributed to i) interaction between the crack front and the particles (crack front curvature model), (ii) deflection of the cracks by the particles before a propagating crack (crack deflection model), and (iii) bridging of cracks by ductile particulates (particulate bridge model). Other secondary mechanisms that contribute to increase the strength of ceramic composites are (iv) the residual stress field (strain) resulting from the difference between the CTE of the ceramic matrix and the particles and (v) grain size[17-19].

In this work, Al_2O_3-$Y_3Al_5O_{12}$ ceramic composites with different contents of $Y_3Al_5O_{12}$ were designed aiming to generate dense materials with outstanding hardness and fracture toughness superior to those of monolithic pure alumina by functionalizing the mechanical strength in the inner layers through particle reinforcement.

2. Experimental Procedure

2.1. Materials

Commercial ceramic powders containing Al_2O_3 (Type – A-3000 SG – Alcoa Aluminio S.A.) and Y_2O_3 (REO – Alfa-Aesar) were used. Nominal chemical compositions. The starting-powders (Al_2O_3 and Y_2O_3) were characterized by X-ray diffraction (XRD) and Scanning Electron Microscopy (SEM), whose details will be presented in the next chapter. The specific surface analysis of the powders was carried out using the Nitrogen Adsorption technique, applying the Brunauer-Emmett- Teller (BET) isotherm as a model. For these analyses, a Micromeritics equipment, model ASAP2020C, was used. The main physical properties (manufacturing data) and results of BET characterizations, are shown in Table 1.

2.2. Processing

Monolithic and multilayer composite specimens were fabricated using five compositions of Al_2O_3 matrix ceramics containing different amounts of Y_2O_3 powder (0, 1, 3, 5 and 10wt.%). To achieve mixture homogenization, ethylic alcohol was added to the powder mixtures and the suspensions were mixed in a mechanical stirrer (NT 137) at 100 rpm for 20 min. Subsequently, the suspensions were dried at 100 °C in a muffle furnace for 24 h. Each powder mixture was deagglomerated using an agate mortar and pestle and then sieved (63 μm mesh). After that, 4wt.% polyvinyl alcohol (PVA)-based organic binder was added to the mixtures. The powder mixtures were homogenized using a planetary ball mill using Al_2O_3 balls and coated vials with Al_2O_3. Finally, monolithic disk specimens (n=10/group) with final dimensions of Ø 20.0 x 2.5 mm were compacted by uniaxial pressing using a pressure of 80 MPa for 60 s.

Multilayer specimens were manufactured in two stages to create compositional gradient: first, the previously compacted disk specimens were added one at a time and pre-compacted so that each new disk containing a lower amount of Y_2O_3 was added until the last layer was formed. For each new disk added, a uniaxial pressure of 20 MPa was applied for 10 s. In the last stage, the complete multilayer specimens were uniaxially pressed at 100 MPa for 60 s. The sintering process for the monolithic and multilayer composite specimens was conducted in a $MoSi_2$ furnace (FORTLAB ME-1800) at 1610 °C for 4 h. The schematic illustration of the sintering thermal cycle and the compaction sequence are shown in Figure 1.

2.3. Characterization

Green density of the compacted specimens was measured by the geometric method using a caliper (repeatability of ±0.01 mm) and analytical balance (repeatability of ±0.001 g).

After sintering, the specimens were ground (45 μm) and automatically polished using the following sequence of diamond pastes (15→9→6→3→1 μm). Apparent density was measured according to Archimedes' principle, and relative density was calculated by correlating the apparent density values with the theoretical density values obtained by the rule of mixtures.

For crystallographic characterization, the polished specimens were analysed at room temperature using a X'Pert PRO

Table 1. Nominal chemical compositions and physical properties of the raw materials used in this work (Suppliers' data).

Al_2O_3		Y_2O_3	
Nominal chemical composition (%)			
Al_2O_3	99.8	Y_2O_3	99.9
Na_2O	0.03	Al_2O_3	< 0.03
MgO	0.040	Fe_2O_3	0.015
SiO_2+CaO+Fe_2O_3	0.045	Ca(ppm)	<0.5
Density (g/cm³)			
3.98		5.01	
Specific surface area (m²/g) - BET measurements			
Al_2O_3		8.595	
Y_2O_3		15.286	
Al_2O_3-1%Y_2O_3		8.871	
Al_2O_3-3%Y_2O_3		10.309	
Al_2O_3-10%Y_2O_3		10.514	

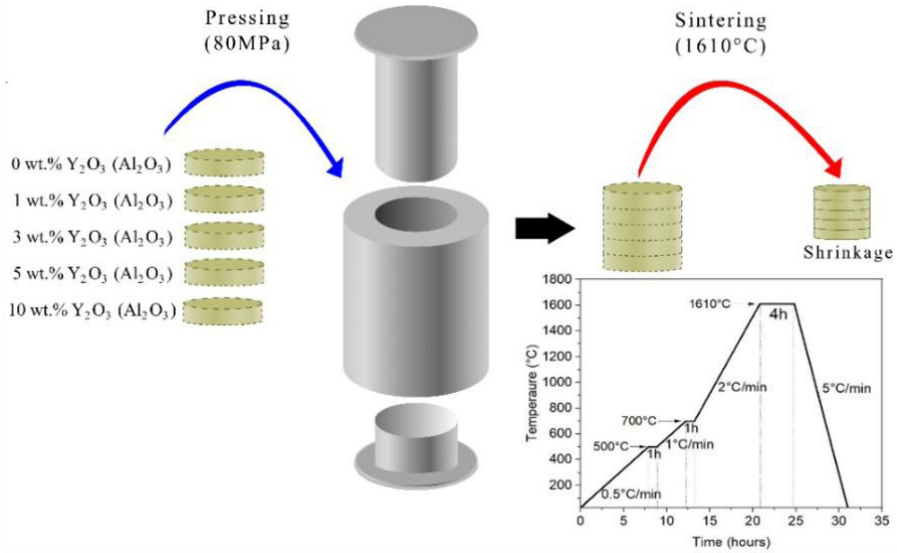

Figure 1. Schematic illustration of the compacted multilayer specimens and the sintering thermal cycle.

Panalytical X-ray diffractometer with a monochromatic CuKα radiation (λ = 0.15418 nm) at 40 kV and 30 mA. Data were measured with 2θ range from 10° to 70°, step size of 0.05°, and counting time of 3 s per step. The phases were identified by comparing the measured diffractograms with standards from Crystallography Open Database (COD) (Al_2O_3, space group: 167 – R$\bar{3}$c with reference code of 96-900-9784) and Inorganic Crystal Structure Database (ICSD) ($YAlO_3$, space group: 62 – Pnma with reference code of 4115, and $Y_3Al_5O_{12}$, space group: 230 – Ia$\bar{3}$d with reference code of 41145).

For microstructural characterization, the polished specimens were thermally etched at 1575 °C for 15 min at a heating rate of 25 °C/min, and a layer of gold was deposited using a K550X sputter coater applying 30 mA for 2 min (Quorum Technologies-UK). The surfaces were evaluated by scanning electron microscopy (SEM/FEG JEOL JSM 7100 F microscope), and grain size (Feret diameter) distribution was measured using the *IMAGE J* software[20].

Fracture toughness and hardness of the specimens were determined using the Vickers indentation method following the ASTM C1327-15 standard[21]. Twenty Vickers indentations were made on the polished surfaces of each layer applying load of 2000 gF (9.8N) for 10 s using a TIME microhardness tester. To analyze the type of crack system acting during crack growth, the model proposed by Casellas *et.al*[22]. is indicated for the Palmqvist crack system, as shown in Equation 1:

$$K_{IC} = 0.0024\left(\frac{E}{HV}\right)^{1/2} \cdot \frac{P}{c^{3/2}} \left(system\ Palmqvist, 0.25 \le \frac{c}{a} \le 2.5\right), \quad (1)$$

where, K_{Ic} is the fracture toughness [MPa.m$^{1/2}$], E is the Young's modulus [GPa], HV is the Vickers hardness [GPa], P is the indentation load [MPa], a is the semi diagonal of Vickers indentation [m], and l is the crack length [m]; "c" = "a + l".

The Young's moduli of the composites were acquired by non-destructive acoustic testing using a Sonelastic detection device allowing ASTM E1876-15 standard[23].

Residual thermal stress was calculated following the models proposed by Shi et al.[24,25], considering the generated thermal difference between the Al_2O_3 matrix and the YAG secondary phase, as shown in Equations 2 and 3. For each composite layer, the respective values of Young's modulus and their CTE were used.

$$\sigma_b = E_b \cdot (\alpha - \alpha_b) \cdot \Delta T, \quad (2)$$

$$\sigma_m = E_m \cdot (\alpha - \alpha_m) \cdot \Delta T', \quad (3)$$

where, respectively, σ_b and σ_m are the residual thermal stresses of the YAG and Al_2O_3 phases; E_b and E_m are the theoretical Young's moduli of YAG (300 GPa) and Al_2O_3 (340 GPa); α, α_b, and α_m are CTE of the composite, YAG (6.14 x 10^{-6} °C^{-1}), and Al_2O_3 (8.5 x 10^{-6} °C^{-1}). The average CTE of the composite was be obtained by Equation 4:

$$\alpha = \frac{\alpha_b C_b E_b + \alpha_m C_m E_m}{C_b E_b + C_m E_m}, \quad (4)$$

where, C_b and C_m are the mole fractions of YAG and Al_2O_3, respectively.

Biaxial flexural strength values of the composites were obtained through piston-on-three balls (P-3B) bending tests[26,27]. In this procedure, a universal testing machine (EMIC DL 1000) was used applying a loading speed of 0.5 mm/min until the specimen ruptured. The flexural strength results were statistically analyzed by the Statistical Power Analysis[28,29].

2.4. Finite element modelling (FEM)

P-3B bending test simulations were performed by 3D finite element simulations, using the ABAQUS/Standard code with static implicit integration technique, assuming isotropic linear-elastic mechanical behavior. Figure 2 presents the proposed 3D FEM model, where the components (disks and

spheres) were meshed with solid elements of reduced linear integration, C3D8R in ABAQUS terminology. A mapped mesh was adopted, more refined in the center of the disk and in the contact zones with the support spheres. The disk, representative of the samples, has 20 layers in a thickness of 58,160 elements and each 1/4 of the spheres is composed of 6,448 /elements, resulting in a total of 71,056 elements. More details are presented in a previous work[30]. Table 2 presents the parameters used in the simulations.

The numerical simulations of the 3B-P tests in Al_2O_3-YAG composites were run in a dual-processor workstation (Intel, Xeon 5690, 3.47 GHz, 24 cores, 32 Gb RAM).

3. Results and Discussion

3.1. Characterization of the raw materials

Figure 3 shows the XRD powder patterns of the raw materials. The diffractograms of both Al_2O_3 (Figure 3a) and Y_2O_3 (Figure 3b) exhibited high crystallinity and no phases other than the matrix were observed. Figure 4 shows the SEM micrographs the powder morphologies of the raw materials.

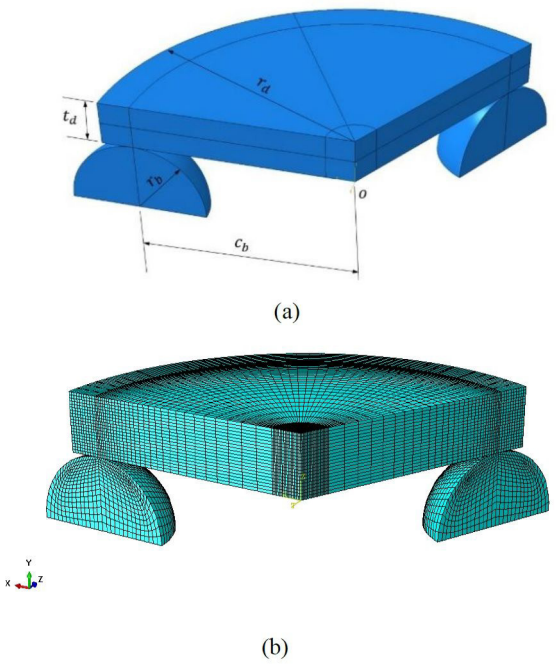

Figure 2. 3D finite-element model simulating P-3B tests proposed: (a) geometrical parameters and (b) meshes of the disc and supporting spherical balls.

Al_2O_3 particles (Figure 4a) presented a quasi-spherical shape and agglomerates or severe aggregates were not observed. Particle size was in the order of 0.65 µm; however, a large number of nanometric particles with sizes <300 nm were detected in the material, which requires further investigation through complementary techniques for confirmation. The Y_2O_3 particles (Figure 4b) exhibited morphological characteristics different from those of the Al_2O_3 particles. A homogeneous elongated tending to acicular aspect was observed, and large agglomerates were not found. The average particle size was slightly higher than that of the alumina particles, presenting an aspect ratio >3.

3.2. Characterization of the compacted specimens

Table 3 shows the theoretical, green and relative green density values of the monolithic specimens. Despite the additions of different amounts of Y_2O_3 to each specimen, the level of compaction of the green density remained constant for each composition, which suggests that the content of 4% binder hindered compositional effects. Moreover, all layers of the multilayer composite compacted specimen exhibited the same relative green density (46.5%).

3.3. Characterization of the sintered specimens

3.3.1. Monolithic specimens

Figure 5 shows the XRD patterns of the monolithic sintered specimens. For all specimens, peaks of α-Al_2O_3[31] were

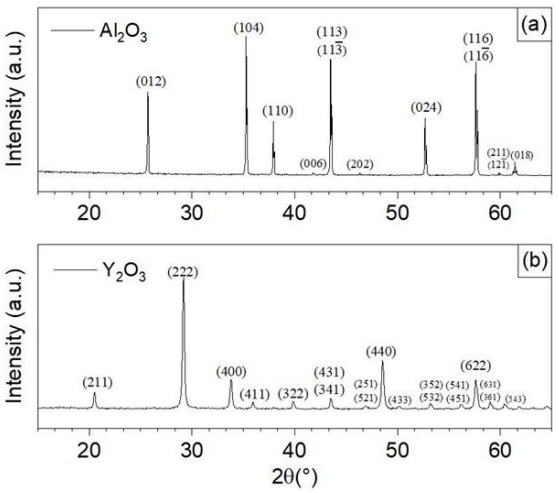

Figure 3. Diffractograms of the raw materials: (a) Al_2O_3 and (b) Y_2O_3.

Table 2. Parameters used in the numerical simulation of the P-3B tests.

Material	Area (mm^2)	Pressure (MPa)	poisson Ratio	Modulus of Elasticity (MPa)
Al_2O_3	1.53938	122.02	0.2200	340000
Al_2O_3 - 1.1 YAG		124.30	0.2203	305900
Al_2O_3 - 5.2 YAG		179.29	0.2216	337920
Al_2O_3 - 7.6 YAG		184.61	0.2223	336960
Al_2O_3 - 13.9 YAG		179.44	0.2242	334400

Table 3. Theoretical, green and relative green density values of the monolithic specimens with addition of different amounts of Y_2O_3

Compositions	Al_2O_3	Al_2O_3 1wt.% Y_2O_3	Al_2O_3 3wt.% Y_2O_3	Al_2O_3 5wt.% Y_2O_3	Al_2O_3 10wt.% Y_2O_3
Theoretical density (g/cm³)	3.98	3.99	4.00	4.01	4.04
Green density (g/cm³)	1.86 ±0.39	1.82 ±0.79	1.88 ±0.12	1.84 ±0.35	1.86 ±0.23
Relative green density (%)	46.8 ±5.3	45.6 ±1.9	47.1 ±3.9	45.9 ±4.1	46.1 ±2.4

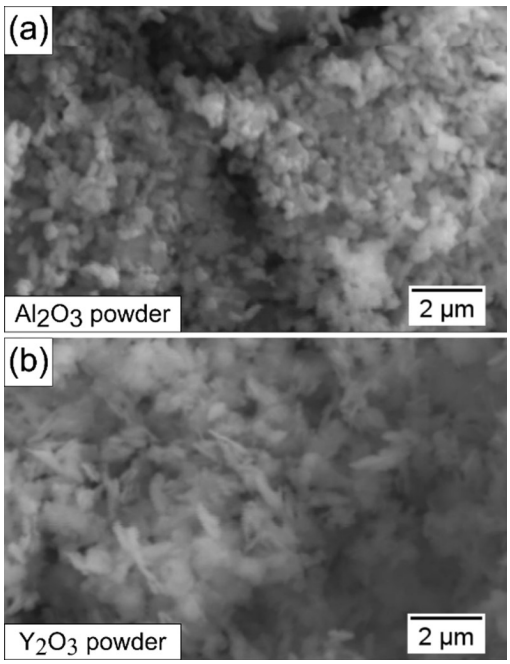

Figure 4. SEM micrographs showing the powder morphology of the raw materials: (a) Al_2O_3 and (b) Y_2O_3.

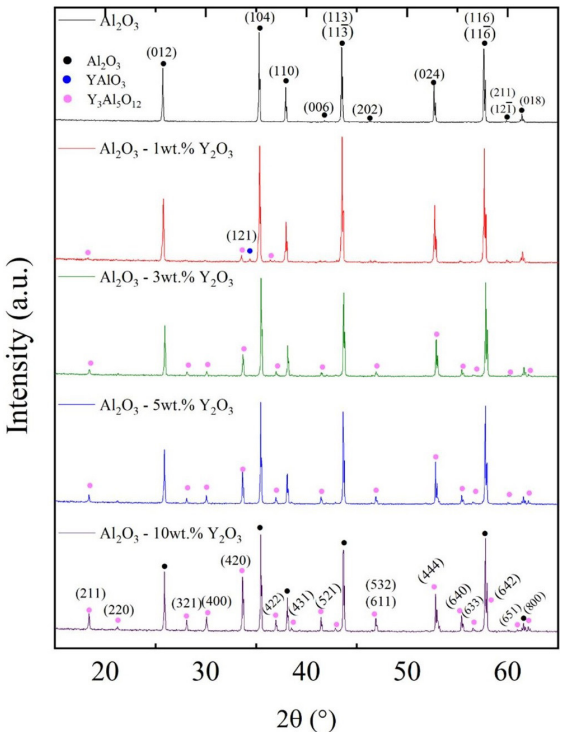

Figure 5. XRD patterns of the monolithic sintered specimens containing 0, 1, 3, 5 and 10wt.% Y_2O_3.

detected, and peaks of the $Y_3Al_5O_{12}$ (YAG)[32] phase were observed for specimens with different contents of Y_2O_3, indicating the existence of the solid-state reaction between Al_2O_3 and Y_2O_3 to form $Y_3Al_5O_{12}$, as shown by the chemical reaction: $5/2Al_2O_3 + 3/2Y_2O_3 \rightarrow Y_3Al_5O_{12}$. In addition, a peak of the intermediate $YAlO_3$[33] phase can be observed for the specimen with 1wt.% Y_2O_3.

A quantitative analysis of the percentage of phases obtained through the Rietveld refinement confirms that the formation of YAG in the layers is proportional to the amount of Y_2O_3 in the mixture, as presented in Table 4. Thus, the addition of 10wt.% Y_2O_3 resulted in the formation of 13.9% YAG - the highest for all specimens, as shown in Figure 6. Furthermore, after sintering, no significant variation in the lattice parameters of both crystalline phases (Al_2O_3 and $Y_3Al_5O_{12}$) was detected, indicating that both phases have structural stability, regardless of the variation in the chemical compositions.

Figure 7a shows the relative density of the of the monolithic specimens with different contents of Y_2O_3. A high densification level can be observed, with values changing progressively between 97.7 ±0.9%, for the pure Al_2O_3 specimen, to 98.6 ±1.0%, for the 10wt.% Y_2O_3 specimen. In terms of relative density, there was no significant variation between the layers, although addition of Y_2O_3 to the Al_2O_3 matrix showed a tendency to increase relative density by ~1%, regardless of the percentage of Y_2O_3 added. Concomitantly with the usual densification steps foreseen for the different solid-phase sintering stages, chemical transformations occurred from reactions in the solid state between Al_2O_3 particles and dispersed Y_2O_3 particles to form the YAG phase; however, this phase transformation did not interfere with the densification of the composites. On the contrary, there was a slight increase in densification that may be related to the difference in diffusivity throughout the grain boundaries of the YAG phase, which may provide, in a limited way, elimination of the residual pores throughout the Al_2O_3-YAG interfaces in the final sintering stage (1610 °C–4h).

The linear and volumetric shrinkage values after sintering for the different compositions are shown in Figure 7b. A tendency to gradually increase shrinkage with increasing the percentage of YAG formed can be observed. Ceramic composites with compositional gradient, such as monolithic ceramics, present elastic (brittle) behavior, and the material does not withstand substantial dimensional variations after

Table 4. Phases, lattice parameters (nm), and amount of phases obtained through the Rietveld refinement of the specimens with addition of 0, 1, 3, 5 and 10wt.% Y_2O_3.

Composition	Phases	Lattice parameters (nm)			Vol (nm^3)	χ^2	Amount (wt.%)
		"a"	"b"	"c"			
Al_2O_3	Al_2O_3	0.476(1)	0.476(1)	1.300(1)	0.255	2.2	100
Al_2O_3 – 1wt.% Y_2O_3	Al_2O_3	0.476(1)	0.476(1)	1.300(0)	0.255	2.6	98.6
	$Y_3Al_5O_{12}$	1.201(4)	1.201(4)	1.201(4)	1.733		1.1
	$YAlO_3$	0.536(8)	0.738(5)	0.517(7)	0.205		0.3
Al_2O_3 – 3wt.% Y_2O_3	Al_2O_3	0.476(1)	0.476(1)	1.300(1)	0.255	2.8	94.8
	$Y_3Al_5O_{12}$	1.201(6)	1.201(6)	1.201(6)	1.735		5.2
Al_2O_3 – 5wt.% Y_2O_3	Al_2O_3	0.476(2)	0.476(2)	1.300(0)	0.255	3.4	92.4
	$Y_3Al_5O_{12}$	1.200(1)	1.200(1)	1.200(1)	1.732		7.6
Al_2O_3 – 10wt.% Y_2O_3	Al_2O_3	0.476(3)	0.476(3)	1.299(9)	0.255	3.9	86.1
	$Y_3Al_5O_{12}$	1.201(3)	1.201(3)	1.201(3)	1.733		13.9

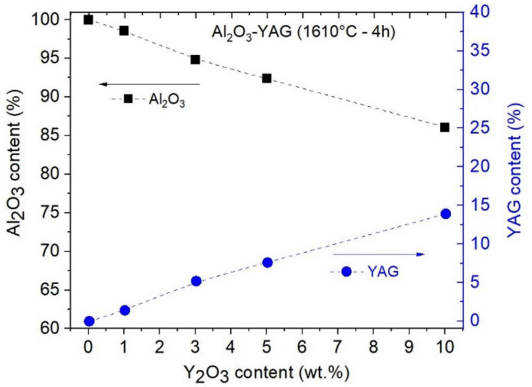

Figure 6. Amount of Al_2O_3 and YAG obtained through Rietveld refinement of the monolithic sintered specimens containing 0, 1, 3, 5 and 10 wt.% Y_2O_3.

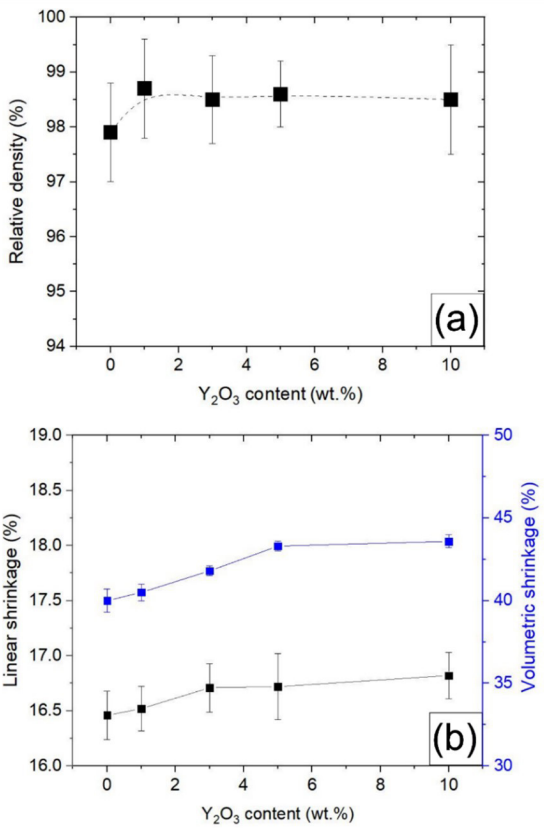

Figure 7. (a) Relative density and (b) linear and volumetric shrinkage of the monolithic sintered specimens containing 0, 1, 3, 5 and 10 wt.% Y_2O_3.

sintering because of the lack of plastic accommodation between the layers[34]. Thus, during the post-sintering cooling process, dimensional differences between the layers should be suppressed or minimized.

3.3.2. Multilayer composite specimens

Figure 8a-e shows the SEM micrographs of the layers in the multilayer composite specimen. For all layers, grains with gray shades represent the Al_2O_3 phase and brighter grains are from the YAG phase. The YAG phase is observed in most of the triple grain junctions of the Al_2O_3 matrix, and it is smaller than the Al_2O_3 grains. As observed in the XRD diffractograms, the amount of YAG increases with increasing the Y_2O_3 content.

Grain size quantifications of the Al_2O_3 and YAG phases are shown in Figure 9a and 9b, respectively. Figure 9a shows grain size distribution curves with a monomodal profile for pure Al_2O_3 and for 1wt.% Y_2O_3 layers, with grain size ranging from 1.5 to 4.0 µm. The curve profile began to change in the 3wt.% Y_2O_3 layer because of the reduction in the average grain size[35]; Figure 9b shows the grain size distribution of the YAG phase of the layers with 3, 5 and 10wt.% Y_2O_3. A monomodal profile with grain size ranging from 0.5 to 1.0 µm was observed for all specimens. As a similar aspect was detected in all compositions, it can be concluded that the YAG grain size distributions do not dependent on the content of Y_2O_3 in the mixture.

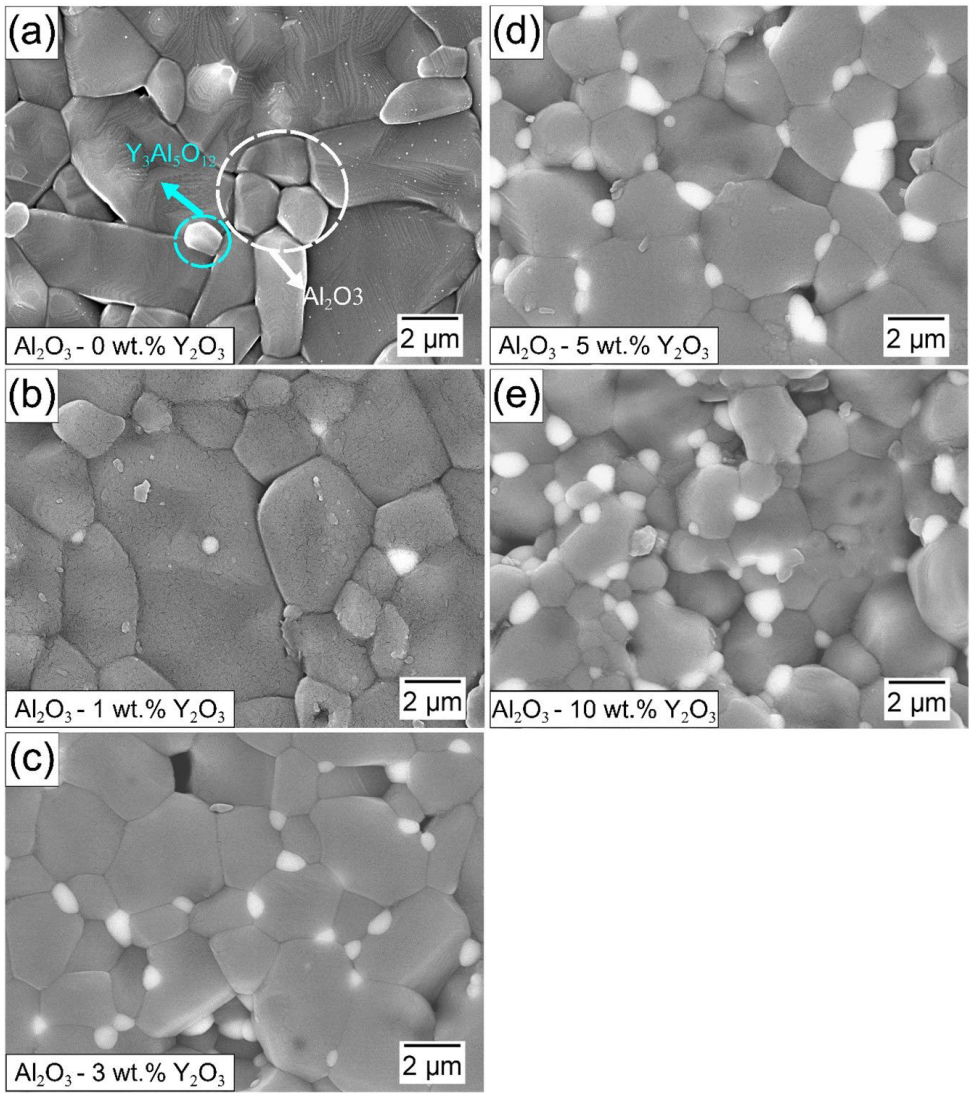

Figure 8. SEM micrographs of multilayer composite sintered specimen: (a) Al_2O_3 – 0wt.% Y_2O_3, (b) Al_2O_3 – 1wt.% Y_2O_3, (c) Al_2O_3 – 3wt.% Y_2O_3, (d) Al_2O_3 – 5wt.% Y_2O_3, and (e) Al_2O_3 – 10wt.% Y_2O_3

The average grain size of the Al_2O_3 phase in relation to the fraction of $Y_3Al_5O_{12}$ is presented in Figure 10. It is observed that the average Al_2O_3 grain size ranges from 3 to 1.25 µm, with an average reduction of 42% between the pure Al_2O_3 layer and the 10wt.% Y_2O_3 layer (~13.9% YAG). These results support the idea of grain size inhibition due to the presence of a second phase during the densification/ grain growth stages.

Therefore, grain growth inhibition can be described as a consequence of two main mechanisms: i) composites that are formed with a stable phase (e.g., α-Al_2O_3) and others formed *in situ* during sintering (e.g., YAG). The initial condition of compaction and, consequently, the contact points between the particles are altered during the chemical reaction in the solid state, where the Y_2O_3 particles are located, thus altering the initial diffusivity conditions of the material. Thus, the start of the activation of the final sintering stages in the solid state of densification and grain growth is delayed, reducing the time required for grain growth in the composites. Consequently, the larger amount of Y_2O_3 in the composition promotes a higher volume of second phase in the material; ii) grain interfaces and triple junctions between Al_2O_3/Al_2O_3 have different atomic mobility compared with the Al_2O_3/$Y_3Al_5O_{12}$ interfaces. Thus, the diffusivity required to enable grain growth is restricted in these regions, limiting the growth of Al_2O_3 grains in the vicinity of new grains formed by YAG. In regions without presence of YAG, the grains can grow easily, as identified in the bimodal profile of the distribution curves shown in Figure 9b.

3.4. Mechanical properties

Figure 11a shows the Vickers hardness and fracture toughness values of the layers in the composite specimen. The pure Al_2O_3 layer exhibited the highest hardness value (1203 HV); meanwhile, the addition of 10wt.% Y_2O_3 reduced the hardness value by 15% (1023 HV) As expected, there is

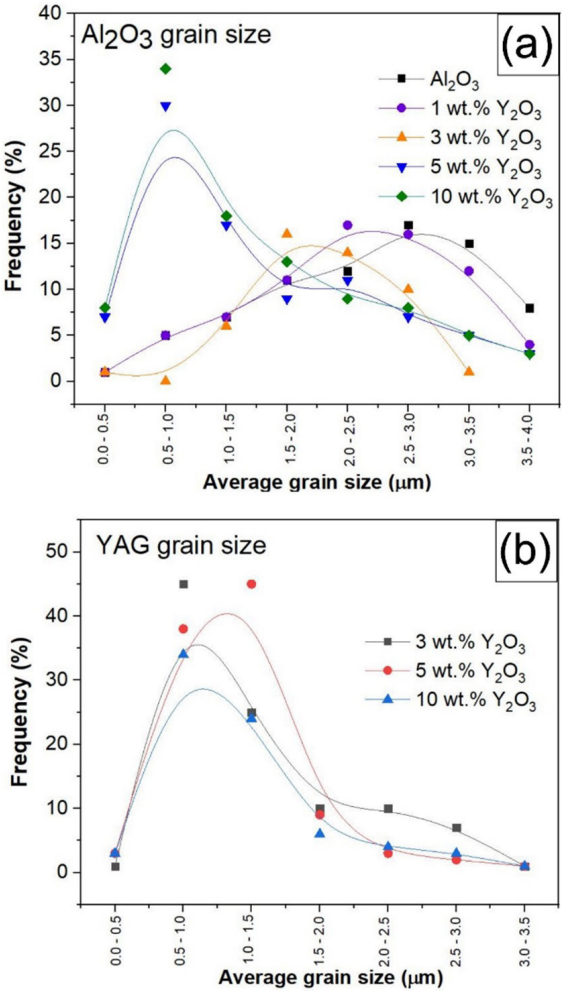

Figure 9. Grain size distribution of (a) Al_2O_3 and (b) YAG.

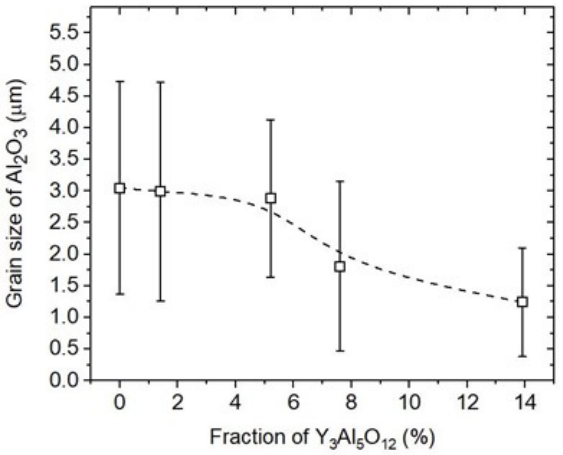

Figure 10. Correlation between Al_2O_3 grain size and YAG content.

a perceptible reduction in hardness between the composite layers. Additionally, the layer overlay resulting from the pre-compression stages allowed a smooth hardness gradient.

Addition of 1wt.% Y_2O_3 did not significantly alter the fracture toughness of the multilayer material, which presents statistically close values of 2.1 ±0.8 MPa.m$^{1/2}$ and 2.0 ±0.5 MPa.m$^{1/2}$ for the pure Al_2O_3 and 1wt.% Y_2O_3 (1.1% YAG) layers, respectively. The similarity between these two layers, especially in terms of Al_2O_3 grain size and relative density, suggests that the main toughening mechanism was crack deflection, and the effects of the second phase on composites with small Y_2O_3 contents were negligible. In contrast, addition of larger amounts of Y_2O_3 starting from 3wt.% resulted in an increase in fracture toughness to 2.7 ±0.6 MPa.m$^{1/2}$, and addition of 10wt.% Y_2O_3 promoted the highest fracture toughness value observed, with improvement of 67%.

The increase in fracture toughness cannot be associated with a decrease in porosity, since no significant variations in the densification of the layers were observed. Thus, the increased resistance to crack propagation in the composite is related to the increase in Y_2O_3 increments in its structure due to formation of the YAG phase during sintering. Therefore, it is suggested that the difference between the coefficient of thermal expansion (CTE) of the two-phase structure (Al_2O_3/YAG) in the composite promoted residual stresses that contributed to increased flexural strength.

Table 5 shows the results of residual thermal stresses developed in the multilayer composites considering ΔT = 1585 ºC. As the α-Al_2O_3 matrix undergoes tensile stresses, the residual stresses acquired values of -3.44 and -161.67 MPa for specimens containing 2.2% and 14% YAG, respectively. In addition, compressive stress values of 1.12 and 0.97 GPa were calculated acting on the secondary YAG phase in these specimens.

Residual thermal stress is an important toughening mechanism in ceramic composites, since the presence of compressive forces between the different phases in the microstructure is a useful barrier to crack propagation with intergranular fracture[20], as shown for the multilayer composite investigated in this work. Figure 11b shows a typical indentation crack exhibiting a preferred intergranular fracture, demonstrating crack deflection during its propagation.

Figure 12 presents the flexural strength as a function of Y_2O_3 content. The results showed that the composite with addition of 1wt.% Y_2O_3 did not achieve a relevant improvement in flexural strength; however, from the content of 3 wt.% Y_2O_3, there is a gain of 68.9 MPa in strength compared with the values of the pure Al_2O_3 - an increase of ~36.7%. Moreover, for the 5 wt.% Y_2O_3 specimen, a gain of 96.4 MPa provided a growth of ~51.3%. Addition of 10 wt.% Y_2O_3 raised flexural strength to 85.8 MPa, resulting in an increase of 45.7% compared with the values of pure Al_2O_3 . Therefore, the gain in strength is associated with formation of the YAG phase because the composite material did not exhibit variation in porosity after sintering.

A power statistical analysis[28,29], Table 6, was used to estimate a minimum sample size at which, with a given confidence level, we should be able to detect an effect. This analysis used a statistical power of 70%, and a significance level of 0.05 and it was able to predict results with an acceptable power level for the type II error. In this study, a power analysis was performed for the case of the t-test of two independent samples, comparing pure Al_2O_3 with the

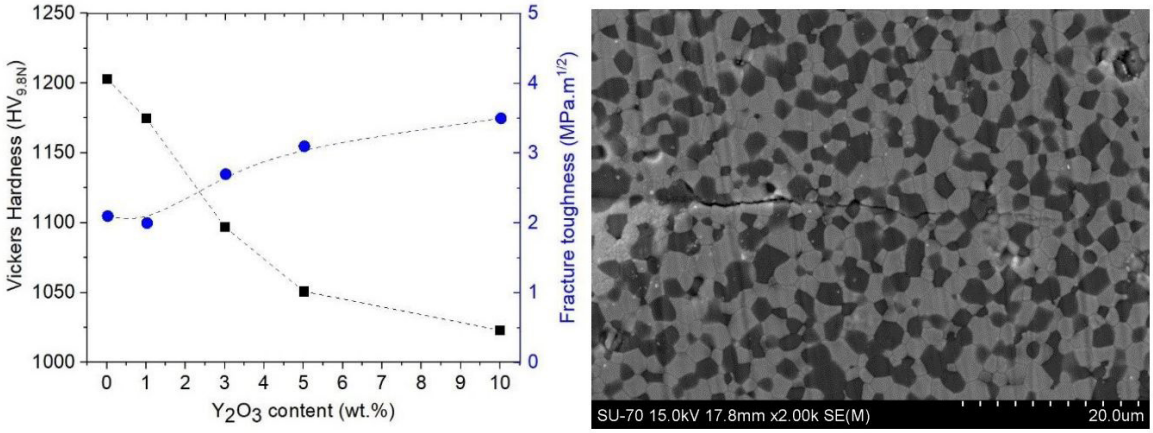

Figure 11. a) Vickers hardness and fracture toughness of the multilayer composite sintered specimen containing 0, 1, 3, 5 and 10 wt.% Y_2O_3; b) Indentation crack growth of the Al_2O_3 – 10wt.% Y_2O_3 specimen (black - alumina grains, gray - YAG grains).

Table 5. Residual thermal stresses developed in the Al_2O_3 and YAG phases in the monolithic sintered specimens with 1, 3, 5 and 10wt.% of Y_2O_3.

Composition	Average CTE	Residual thermal stress of Al_2O_3	Residual thermal stress of YAG
Al_2O_3 – 1wt.% Y_2O_3	8.49 x 10^{-6} °C	- 11.34 x 10^6	1.11 x 10^9
Al_2O_3 – 3wt.% Y_2O_3	8.49 x 10^{-6} °C	- 58.74 x 10^6	1.07 x 10^9
Al_2O_3 – 5wt.% Y_2O_3	8.34 x 10^{-6} °C	- 86.22 x 10^6	1.04 x 10^9
Al_2O_3 – 10wt.% Y_2O_3	8.20 x 10^{-6} °C	- 161.67 x 10^6	0.97 x 10^9

Table 6. Results of statistical analysis comprising three different compositions, containing 3%, 5% or 10% Y_2O_3.

Statistic Powder					
Al_2O_3 3% Y_2O_3					
T	dof	Alternative	Cohen-d	BF10	power
T-test 2.258183	12.099748	two-sided	1.179693	1.983	0.559482
Effect size = 1.179693					
Minimum sample size = 9.92					
Al_2O_3 5% Y_2O_3					
T	dof	Alternative	Cohen-d	BF10	power
T-test 3.599685	8.448362	two-sided	1.891734	9.726	0.871189
Effect size = 1.891734					
Minimum sample size = 4.62					
Al_2O_3 10% Y_2O_3					
T	dof	Alternative	Cohen-d	BF10	power
T-test 3.687098	12	two-sided	1.970837	12.158	0.922094
Effect size = 1.970837					
Minimum sample size = 4.37					

other groups. The t-test calculated a p-value that interpreted if the samples are the same (fail to reject the null hypothesis), or if there is a statistically significant difference between the samples (reject the null hypothesis). The common measure for comparing the difference in the mean from the groups was Cohen's d measure. This measure calculates a standard score that describes the difference in terms of the number of standard deviations that the means are different.

3.5. Analysis of the Finite Element Method (FEM)

Table 7 summarizes the finite element loading conditions obtained from representative experimental biaxial flexural strength data and Figures 13 and 14 show the distribution of stress components for monolithic alumina and Al_2O_3 composites containing 13.9% YAG, in the radial (S11 in MPa) and circular (S22 in MPa) directions obtained on the lower surface of the disc from the proposed 3D models.

In this study, the biaxial bending is defined as the average value (σ_a) of the radial (σ_r) and circular (σ_θ) stresses determined from the centroid of the 3D hexahedral element located in the center of the disk. As expected, highly compressive stresses can be observed in the contact zones between the spheres and the lower surface of the analyzed ceramic disk. Furthermore, there is a stress state very close to the equi-biaxial tensile condition at the bottom center of the simulated ceramic disc. The behavior of tensile and compressive stresses resulting from the biaxial flexural strength test increased with the maximum experimental piston force, as expected. In the case of ceramics that are notably brittle (Al_2O_3 and YAG), the toughening mechanisms acting on the materials studied here are restricted to residual thermal stresses arising from differences in thermal behavior of the phases present in addition to the traditional crack deflection mechanism, as already seen previously.

As the finite element analysis carried out in the present work uses only the elastic properties defined by Young's modulus and Poisson's coefficient, microstructural parameters and porosity are not considered. The differences in resistance to biaxial bending found between the finite element predictions and the average experimental values for each material, presented in Table 7, are of the order of 40%, and are mostly attributed to the porosity present in the materials, denounced by the limited relative density of ceramics (Table 3), which outweighs any benefit of possible toughening mechanisms existing in ceramic composites.

When analyzing simulation results that reflect multilayer materials, considering layers of monolithic alumina superimposed on Al_2O_3-13.9%YAG composites, extreme limits of compositional difference investigated in this work, the existing differences shown in Table 8, when monolithic alumina or Al_2O_3-13.9%YAG Composite are positioned on the tensile surface, are negligible in the simulation of bending tests. This indicates, in a preliminary character. that both layers, positioned in an extreme way in multilayer composites containing between 0% and 10% of Y_2O_3 as raw material, do not interfere in a considerable way in the final flexural strength of the composite, while the fracture toughness of the composite is superior in the layer of the composite than in monolithic alumina, as expected.

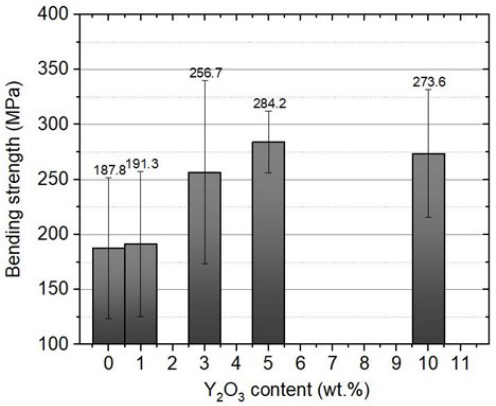

Figure 12. Bending strength of the monolithic sintered specimens containing 0, 1, 3, 5 and 10 wt.% Y_2O_3.

Table 7. Numerical predictions and experimental values regarding the biaxial flexural strength of the Al_2O_3-YAG ceramic composites.

Composition	σ_a (MPa)	s11	s22	σ_f (MPa)	Diference (%)
		σ_r (MPa)	σ_θ (MPa)		
Al_2O_3	187.84	148,72	61,12	104.92	44.1
Al_2O_3 - 1.1%YAG	191.35	150,85	61,02	105.93	44.6
Al_2O_3 - 5.2% YAG	275.99	216,61	78,3	147.45	46.7
Al_2O_3 - 7.6% YAG	284.19	222,95	79,5	151.22	46.8
Al_2O_3 - 13.9% YAG	276.23	217,2	78,12	147.66	46.5

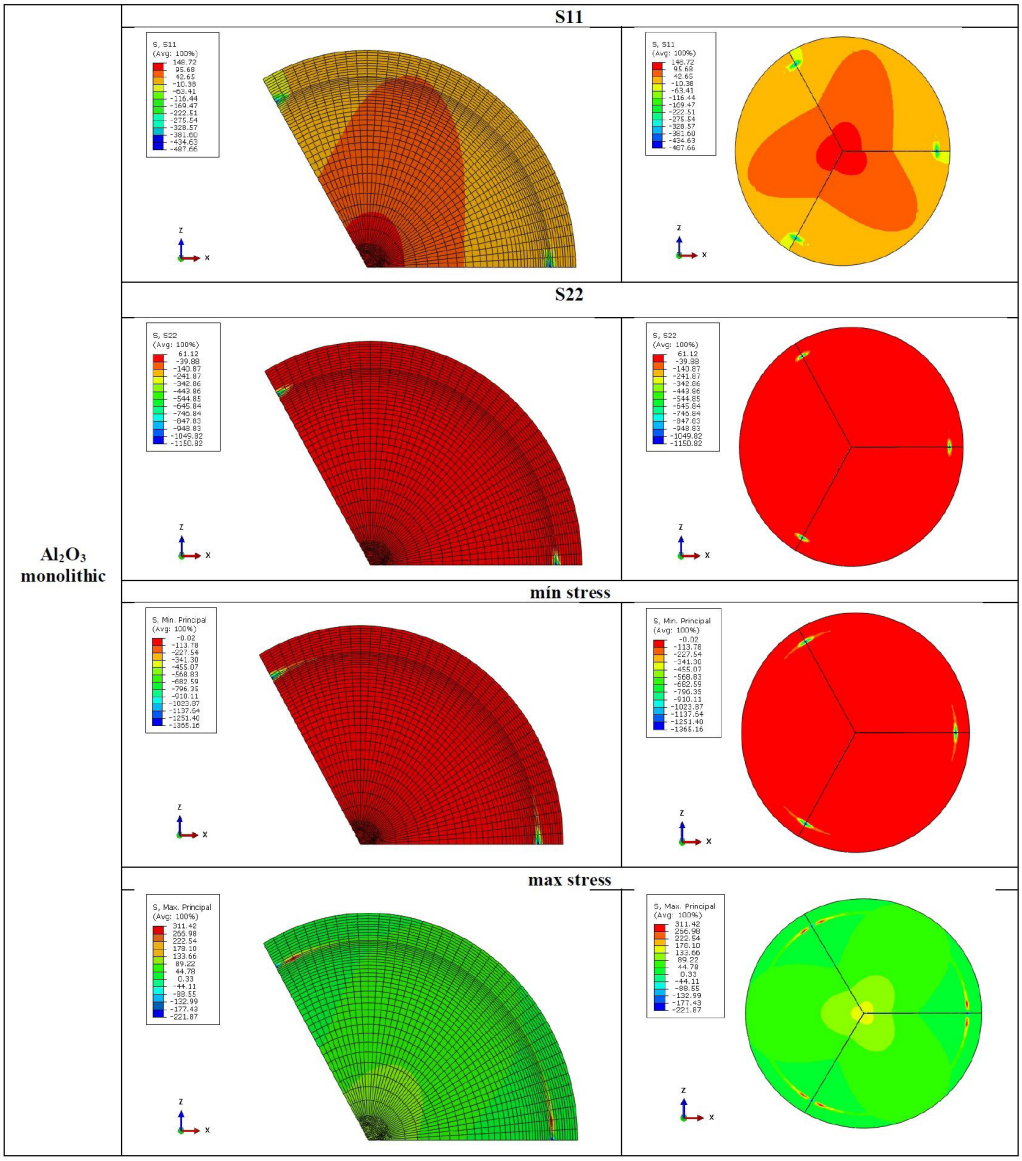

Figure 13. Contour plots of radial (S11 in MPa) and circular (S22 in MPa) stress at the bottom of sample disks determined from finite element simulations of the biaxial bending test of monolithic alumina.

Table 8. Results of P-3B test simulations on multilayer discs.

Simulation Condition	Experimental Stress adopted	Radial Stress	Circumferential Stress	Mean Stress	Diference (%)
Monolithic Al_2O_3 (Top side) Al_2O_3-13.9%YAG (down - tensile)	187.84	147.96	60.96	104.46	44.39
Al_2O_3-13.9%YAG (Top side) Monolithic Al_2O_3 (down - tensile)	187.84	149.40	61.20	105.3	43.94

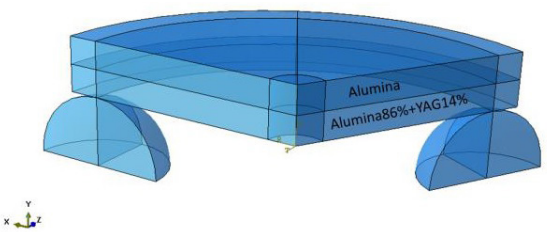

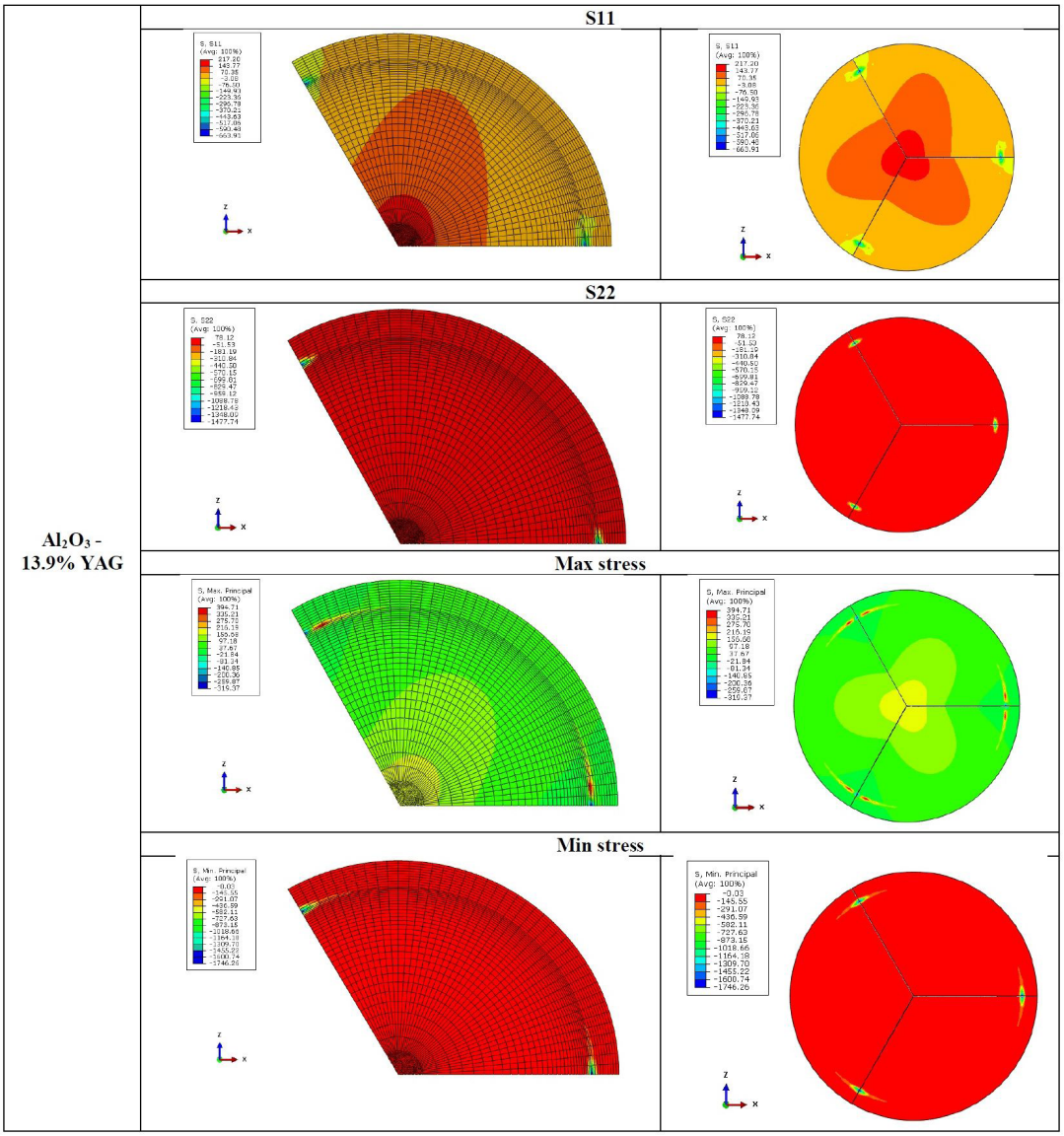

Figure 14. Radial (S11 in MPa) and circular (S22 in MPa) stress contour plots at the bottom of the sample discs determined from the finite element simulations of the biaxial bending test of the Al_2O_3-13.9%YAG composite.

4. Conclusions

Ceramic composites based on Al_2O_3 with levels of $Y_3Al_5O_{12}$ varying between 1.1 and 13.9% as reinforcement showed compatible shrinkage between the layers after sintering. During sintering, the inhibition in the growth of alumina grains with increasing the Y_2O_3 content, associated with the increase in densification and the thermal compatibility between the crystalline phases of the sintered samples allowed the average values of flexural strength (187.8 MPa) and fracture toughness (2.1 MPa.m$^{1/2}$) of pure alumina, were significantly improved, reaching average values of 273.6 MPa, and 3.5 MPa. m$^{1/2}$ for the highest reinforcement content studied in this work (Al_2O_3- 13.9% YAG). The presence of compositional gradients between layers, which result in composites with different microstructural characteristics, providing significant gains in mechanical strength and fracture toughness compared to monolithic alumina, may make this material viable for future structural applications where hardness and toughness are mandatory combined properties for the technical success of these ceramic composites.

5. Acknowledgments

The authors would like to thank the LABNANO/CBPF for the technical support with the electron microscopy analyses, besides INPE and UNIVAP by BET measurements. Dr. Claudinei Santos acknowledges FAPERJ (grant E26-202.997/2017) and CNPq (grant 311119/2017-4).

6. References

1. Dörre E, Hübner H. Alumina: processing, properties, and applications. Berlin: Springer; 1984.

2. Ruys A. Alumina ceramics: biomedical and clinical applications. Oxford: Woodhead Publishing; 2019.
3. Liu B, Li J, Ivanov M, Liu W, Liu J, Xie T, et al. Solid-state reactive sintering of Nd:YAG transparent ceramics: the effect of Y_2O_3 powders pre treatment. Opt Mater. 2014;36(9):1591-7. http://dx.doi.org/10.1016/j.optmat.2014.04.038.
4. Mah T, Parthasarathy TA, Matson LE. Processing and mechanical properties of $Al_2O_3/Y_3Al_5O_{12}$ (YAG) eutectic composite. Ceram Eng Sci Proc. 1990;11:1617-27. http://dx.doi.org/10.1002/9780470313053.ch36.
5. Paneto FJ, Pereira JL, Lima JO, Jesus EJ, Silva LA, Sousa Lima E, et al. Effect of porosity on hardness of Al_2O_3–$Y_3Al_5O_{12}$ ceramic composite. Int J Refract Hard Met. 2015;48:365-8. http://dx.doi.org/10.1016/j.ijrmhm.2014.09.010.
6. Korte C, Franz B. Reaction kinetics in the system Y_2O_3/Al_2O_3: a solid state reaction forming multiple product phases investigated by using thin film techniques. Solid State Ion. 2021;368:115699. http://dx.doi.org/10.1016/j.ssi.2021.115699.
7. Ochiai S, Ueda T, Sato K, Hojo M, Waku Y, Nakagawa N, et al. Deformation and fracture behavior of an Al_2O_3/YAG composite from room temperature to 2023 K. Compos Sci Technol. 2001;61(14):2117-28. http://dx.doi.org/10.1016/S0266-3538(01)00159-2.
8. Su H, Zhang J, Liu L, Fu H. Processing, microstructure, and properties of laser remelted $Al_2O_3/Y_3Al_5O_{12}$(YAG) eutectic in situ composite. Trans Nonferrous Met Soc China. 2007;17(6):1259-64. http://dx.doi.org/10.1016/S1003-6326(07)60259-3.
9. Bučevac D, Omerašević M, Egelja A, Radovanović Ž, Kljajević L, Nenadović S. Effect of YAG content on creep resistance and mechanical properties of Al_2O_3-YAG composite. Ceram Int. 2020;46(10):15998-6007. http://dx.doi.org/10.1016/j.ceramint.2020.03.150.
10. Harada Y, Suzuki T, Hirano K, Waku Y. Ultra-high temperature compressive creep behavior of an in-situ Al_2O_3 single-crystal/YAG eutectic composite. J Eur Ceram Soc. 2004;24(8):2215-22. http://dx.doi.org/10.1016/S0955-2219(03)00640-X.
11. Palmero P, Fantozzi G, Lomello F, Bonnefont G, Montanaro L. Creep behaviour of alumina/YAG composites prepared by different sintering routes. Ceram Int. 2012;38(1):433-41. http://dx.doi.org/10.1016/j.ceramint.2011.07.024.
12. Xia Z, Li L. Understanding interfaces and mechanical properties of ceramic matrix composites. In: Low IM, editor. Advances in ceramic matrix composites. Cambridge: Woodhead Publishing; 2014. p. 267-85. http://dx.doi.org/10.1533/9780857098825.2.267
13. Lima ES, Itaboray LM, Santos APO, Santos C, Cabral RF. Mechanical properties evaluation of Al_2O_3-YAG ceramic composites. Mater Sci Forum. 2015;820:239-43. http://dx.doi.org/10.4028/www.scientific.net/MSF.820.239.
14. Alves M, Abreu LG, Klippel GGP, Santos C, Strecker K. Mechanical properties and translucency of a multi-layered zirconia with color gradient for dental applications. Ceram Int. 2021;47(1):301-9. http://dx.doi.org/10.1016/j.ceramint.2020.08.134.
15. Santos C, Cossu CMFA, Alves MFRP, Campos LQB, Magnago RO, Strecker K. Al_2O_3/Y-TZP ceramic composite with unidirectional functional gradient. Int J Refract Hard Met. 2018;75:147-52. http://dx.doi.org/10.1016/j.ijrmhm.2018.03.008.
16. Kieback B, Neubrand A, Riedel H. Processing techniques for functionally graded materials. Mater Sci Eng A. 2003;362(1-2):81-106. http://dx.doi.org/10.1016/S0921-5093(03)00578-1.
17. Fan K, Pastor JY, Ruiz-Hervias J, Gurauskis J, Baudin C. Determination of mechanical properties of Al_2O_3/Y-TZP ceramic composites: influence of testing method and residual stresses. Ceram Int. 2016;42(16):18700-10. http://dx.doi.org/10.1016/j.ceramint.2016.09.008.
18. Taya M, Hayashi S, Kobayashi AS, Yoon HS. Toughening of a particulate-reinforced ceramic-matrix composite by thermal residual stress. J Am Ceram Soc. 1990;73(5):1382-91. http://dx.doi.org/10.1111/j.1151-2916.1990.tb05209.x.
19. Aharonian C, Tessier-Doyen N, Geffroy P-M, Pagnoux C. Elaboration and mechanical properties of monolithic and multilayer mullite-alumina based composites devoted to ballistic applications. Ceram Int. 2021;47(3):3826-32. http://dx.doi.org/10.1016/j.ceramint.2020.09.242.
20. Lau M, Morgenstern F, Hübscher R, Knospe A, Herrmann M, Döring M, et al. Image segmentation variants for semi-automated quantitative microstructural analysis with ImageJ. Prakt Metallogr. 2020;57(11):752-75. http://dx.doi.org/10.3139/147.110626.
21. ASTM: American Society for Testing and Materials. ASTM: C 1327-15: standard test method for vickers indentation hardness of advanced ceramics. West Conshohocken: ASTM; 2015. 10 p.
22. Casellas D, Ràfols I, Llanes L, Anglada M. Fracture toughness of zirconia alumina composites. Int J Refract Hard Met. 1999;17(1-3):11-20. http://dx.doi.org/10.1016/S0263-4368(98)00064-X.
23. ASTM: American Society for Testing and Materials. ASTM E1876-15, "Standard test method for dynamic Young's modulus, shear modulus, and Poisson's ratio by impulse excitation of vibration. West Conshohocken: ASTM; 2015.
24. Shi JL, Lu ZL, Guo JK. Model analysis of boundary residual stress and its effect on toughness in thin boundary layered yttria-stabilized tetragonal zirconia polycrystalline ceramics. J Mater Res. 2000;15(3):727-32. http://dx.doi.org/10.1557/JMR.2000.0105.
25. Shi JL, Li L, Guo JK. Boundary stress and its effect on toughness in thin boundary layered and particulate composites: model analysis and experimental test on T-TZP, based ceramic composites. J Eur Ceram Soc. 1998;18(14):2035-43. http://dx.doi.org/10.1016/S0955-2219(98)00157-5.
26. Wachtman JB, Cappa W, Mandel J. Biaxial flexure tests of ceramic substrates. J Mater. 1972;7(2):188-94.
27. ISO: International Organization for Standardization. ISO 6872-15: dentistry: ceramic materials. 4th ed. Geneva: ISO; 2015. 28 p.
28. Jones SR, Carley S, Harrison M. An introduction to power and sample size estimation. Emerg Med J. 2003;20(5):453-8. http://dx.doi.org/10.1136/emj.20.5.453.
29. Cohen J. Statistical power analysis. Curr Dir Psychol Sci. 1992;1(3):98-101. http://dx.doi.org/10.1111/1467-8721.ep10768783.
30. Coutinho IF, Silva PC, Moreira LP, Strecker K, Alves MFRP, Santos C. Experimental analysis and numerical simulations of the mechanical properties of a (Ce,Y)-TZP/Al_2O_3/H6A ceramic composite containing coupled toughening mechanisms. J Mech Behav Biomed Mater. 2022;129:105171. http://dx.doi.org/10.1016/j.jmbbm.2022.105171.
31. Pauling L, Hendricks SB. The cystal structures of hematite and corundum. J Am Chem Soc. 1925;47:781-90. http://dx.doi.org/10.1021/ja01680a027.
32. Bagdasarov KS, Bolotina NB, Kalinin VI, Karyagin VF, Kuz'min BV, Muradyan LA, et al. Photoinduced effects and real structure of crystals of yttrium aluminum garnet. Kristallografiya. 1991;36:398-405.
33. Diehl R, Brandt G. Crystal structure refinement of $YAlO_3$, a promising laser material. Mater Res Bull. 1975;10(2):85-90. http://dx.doi.org/10.1016/0025-5408(75)90125-7.
34. Suresh S. Modeling and design of multi-layered and graded materials. Prog Mater Sci. 1997;42(1-4):243-51. http://dx.doi.org/10.1016/S0079-6425(97)00017-0.
35. Hillert M. Inhibition of grain growth by second-phase particles. Acta Metall. 1988;36(12):3177-81. http://dx.doi.org/10.1016/0001-6160(88)90053-3.